Supplement:

Organic sulfur fluxes and geomorphic control of sulfur isotope ratios in rivers

Preston C. Kemeny[a*], Mark A. Torres[b], Michael P. Lamb[a], Samuel M. Webb[c], Nathan Dalleska[a], Trevor Cole[b], Yi Hou[b], Jared Marske[a], Jess F. Adkins[a], Woodward W. Fischer[a]

[a] Geological and Planetary Sciences, California Institute of Technology, Pasadena, CA, USA
[b] Earth, Environmental, and Planetary Sciences, Rice University, Houston, TX, USA
[c] Stanford Synchrotron Radiation Lightsource, SLAC National Accelerator Laboratory, Menlo Park, CA, USA

[*]Corresponding author: pkemeny@caltech.edu, preston.kemeny@gmail.com

Appendices

Tables

Figures

Appendix A. Images of the Efri Haukadalsá catchment

Images of the Efri Haukadalsá catchment were collected by drone (Fig. A.1), hand-held photography (Fig. A.2), and satellite (Fig. A.3).

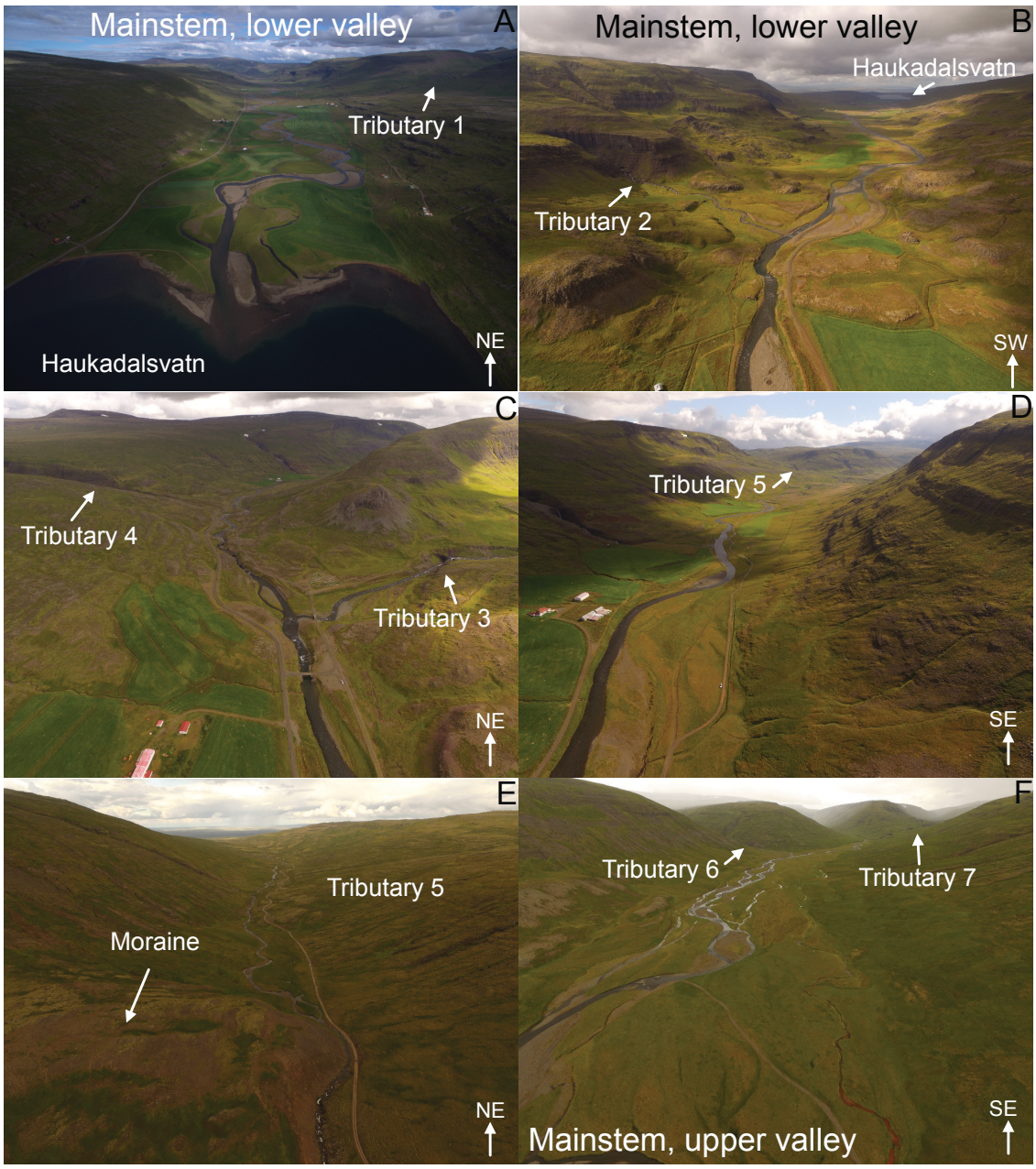

Fig. A.1. Drone images of the Efri Haukadalsá catchment. (A) The lower valley of the catchment viewed from the mouth of Haukadalsvatn and (B) from slightly upstream of the confluence with tributary 2. (C) Confluence of tributary 3 with the Efri Haukadalsá, with tributary 4 also visible. (D) The Efri Haukadalsá between the two knickzones. (E) Tributary 5, which partially drains the moraine. (F) The upper valley of the catchment, with tributary 6 and tributary 7 visible. Arrows in bottom right of each panel indicate approximate image orientation.

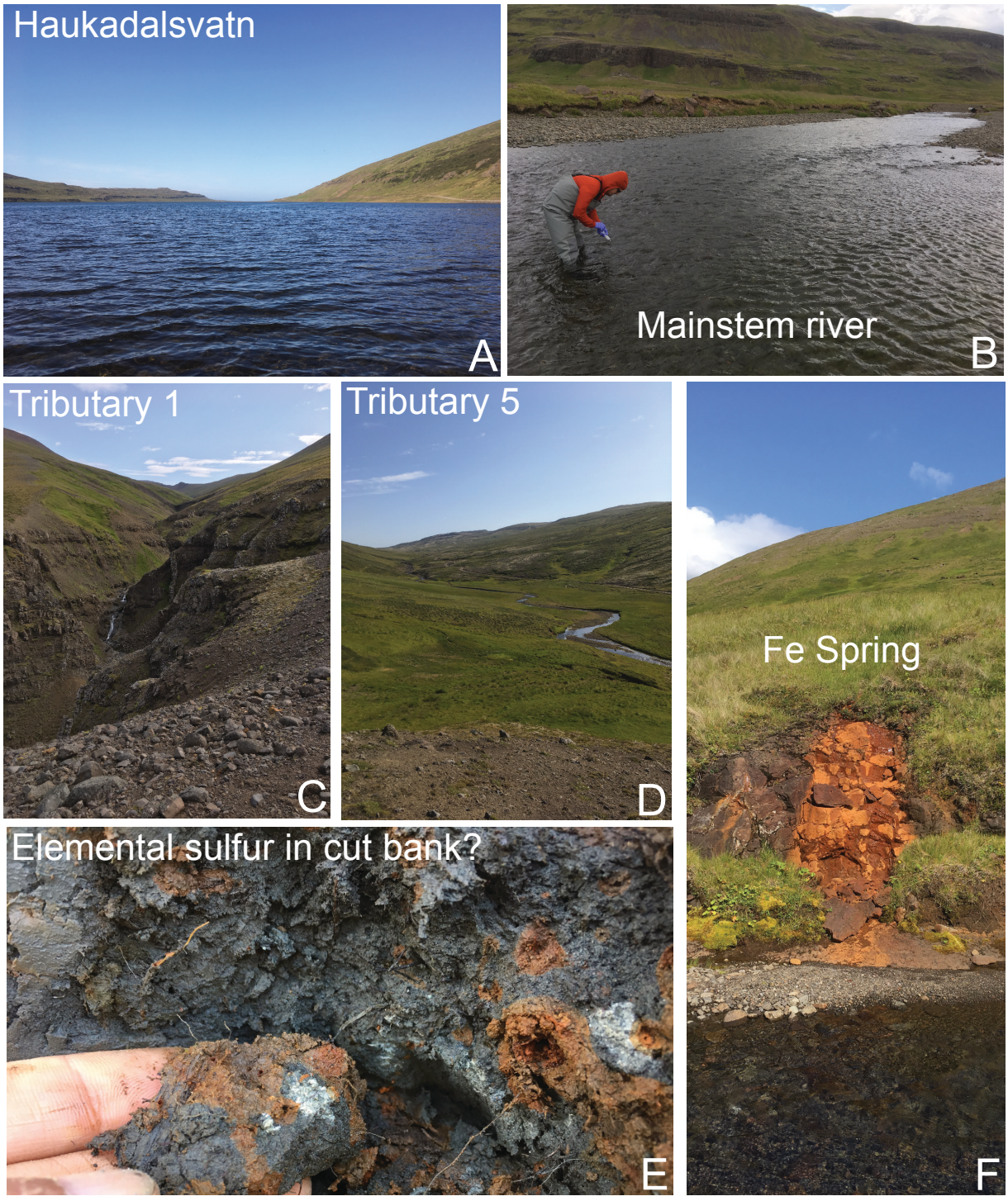

Fig. A.2. Photographs of the Efri Haukadalsá catchment. (A) Lake Haukadalsvatn viewed from the junction with the Efri Haukadalsá. (B) Collecting a water sample from the mainstem river. The person in this image is ~ 2 m tall. (C) Tributary 1, several hundred meters upstream of the confluence with the mainstem. (D) Tributary 5, as seen from the moraine. (E) The smell of white material observed in a cutbank of the lower valley suggested sulfur, but this was not experimentally confirmed. (F) Example of a Fe spring, which are found throughout the Efri Haukadalsá catchment.

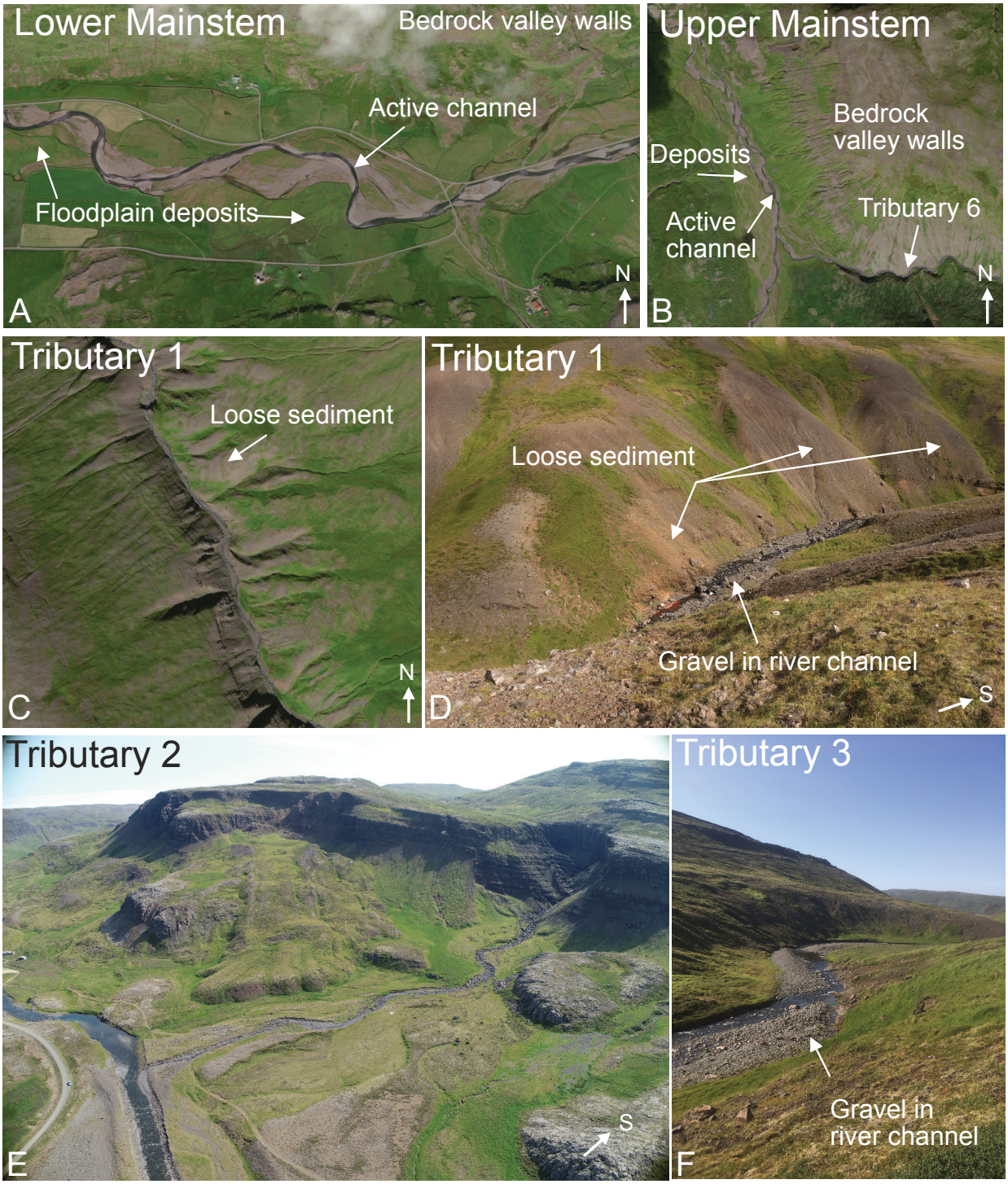

Fig. A.3. (A, B, C) Satellite images from Google Earth and (D, E, F) drone and hand-held photographs of tributaries in the Efri Haukadalsá catchment. (A) The lower mainstem river with floodplain deposits and bedrock valley walls. In this reach the Efri Haukadalsá is a meandering, alluvial river with wide floodplain disconnected from bedrock sources. (B) The upper mainstem river. (C) Satellite and (D) hand-held photograph of tributary 1 with loose sediment and gravel in the river channel. (E) Drone photograph of tributary 2 and (F) hand-held photograph of tributary 3. Arrows in the bottom-right of each panel indicate approximate image orientation.

Appendix B. Chromatography measurements of cation concentration

During collection, one split of each river water sample was acidified with concentrated high-purity HNO_3 to prevent adsorption of ions to container walls and precipitation of secondary phases. This acidified split was then measured by ion chromatography to quantify [Ca^{2+}], [Mg^{2+}], [Na^{+}], and [K^{+}]. A subset of acidified samples was measured on the same run as both acidified and non-acidified calibration solutions, a subset was measured with only acidified solutions, and a final subset was measured with only non-acidified calibration solutions. For samples measured with both acidified and non-acidified solutions, the calibrated values were extremely similar when calibrated with acidified or unacidified solutions (Fig. B.1A). The fractional difference between values calibrated using acidified or non-acidified calibration solutions was < 2% for Ca^{2+}, Na^{+}, and Mg^{2+} (Fig. B.1B). The difference was larger for K^{+}, closer to ~5-10%, but the absolute change was less than ~1 μM due to the very low [K^{+}] values of the samples (Fig. B.1B). The proportional offset between the two sets of calibrated values was related to the sample dilution factor, suggesting that the cause of the variation was the acid content of each solution. Where available, we reported measurements of acidified samples calibrated with acidified calibration solutions.

There was no acidified split collected for several precipitation samples due to insufficient volume. To test if cations measurements could be made on the unacidified split, we measured the acidified and unacidified splits of other precipitation, snow, and ice samples in the same run as both acidified and unacidified calibration solutions. As found for river water samples, the calibrated values of [Ca^{2+}], [Mg^{2+}], [Na^{+}], and [K^{+}] in acidified samples were extremely similar when calibrated with acidified or unacidified calibration solutions (Fig. B.1C). However, there were differences when comparing the acidified samples calibrated with acidified solutions to the unacidified samples

calibrated with unacidified solutions (Fig. B.1D). Because the deviation of calibrated values was to both sides of the 1:1 line, the discrepancy was not clearly attributed to either a blank associated with the added HNO_3, adsorption of ions to container walls, or precipitation of secondary phases. Overall, we do not report cation concentrations measured on unacidified samples.

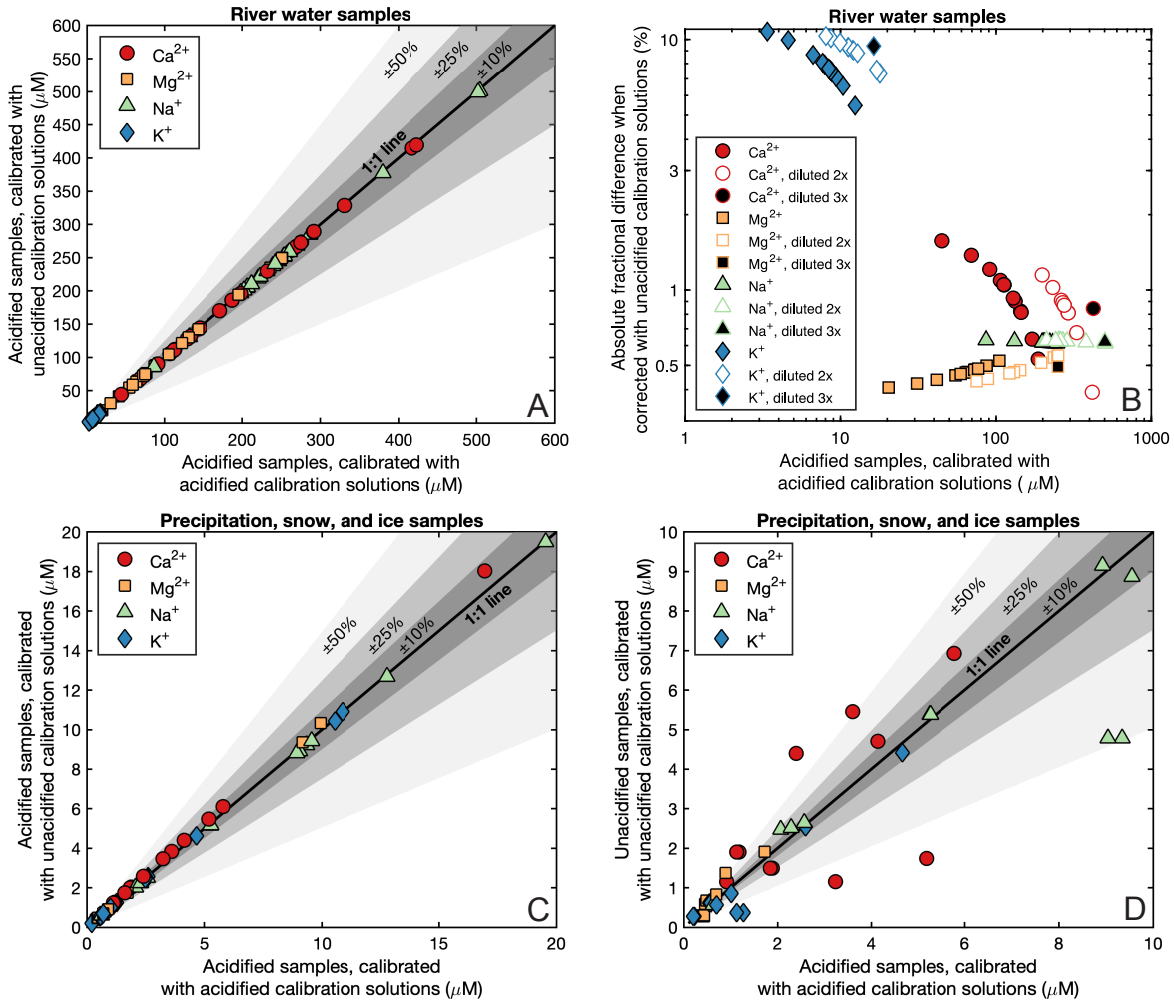

Fig. B.1. Cation chromatography measurements. (A) $[Ca^{2+}]$, $[Mg^{2+}]$, $[Na^+]$, and $[K^+]$ determined on acidified river water samples calibrated with either acidified or unacidified calibration solutions. (B) The fractional difference of the two determinations was minimal for all cations other than K^+, where the absolute difference was minimal (~1 μM). (C) $[Ca^{2+}]$, $[Mg^{2+}]$, $[Na^+]$, and $[K^+]$ determined on acidified precipitation, snow, and ice samples calibrated with either acidified or unacidified calibration solutions. (D) The calibrated values of $[Ca^{2+}]$, $[Mg^{2+}]$, $[Na^+]$, and $[K^+]$ determined on unacidified precipitation, snow, and ice samples calibrated with unacidified solutions plotted against values determined on acidified precipitation, snow, and ice samples calibrated with acidified solutions. The lack of agreement between the acidified and unacidified samples precludes using unacidified splits of precipitation samples to quantify $[Ca^{2+}]$, $[Mg^{2+}]$, $[Na^+]$, and $[K^+]$ in cases where no acidified split was collected.

Appendix C. Synchrotron filter blank and vegetation mapping

Suspended sediment from the Efri Haukadalsá was filtered onto combusted Glass Fiber Filters. Subsequently, multiple-energy mapping of an unwashed, blank filter at the SLAC National Accelerator Laboratory identified abundant sulfur (Torres et al., 2020). The flourescence response was strong at 2481.0 eV and 2482.5 eV, with no coherent response at the incident energies characteristic of reduced sulfur moities. X-ray absorption spectra of the blank filter were consistent with sulfate and a variable contribution from sulfonate. We note that, if this blank was present in our synchrotron measurements, it could only have existed in observations of supended sediment because X-ray absorption spectra of deposit and vegetation samples were collected directly on raw materials. As argued previously in Torres et al. (2020), the sulfur blank on the filters used to sample suspended sediment was highly soluble and likely rinsed off during filtration; a blank filter rinsed lightly with water showed a substantially lower flourscence response than an unwashed filter. Moreover, due to attenuation of the incoming X-ray beam, the incident beam was unlikely to penetrate through the sample to the underlying fitler.

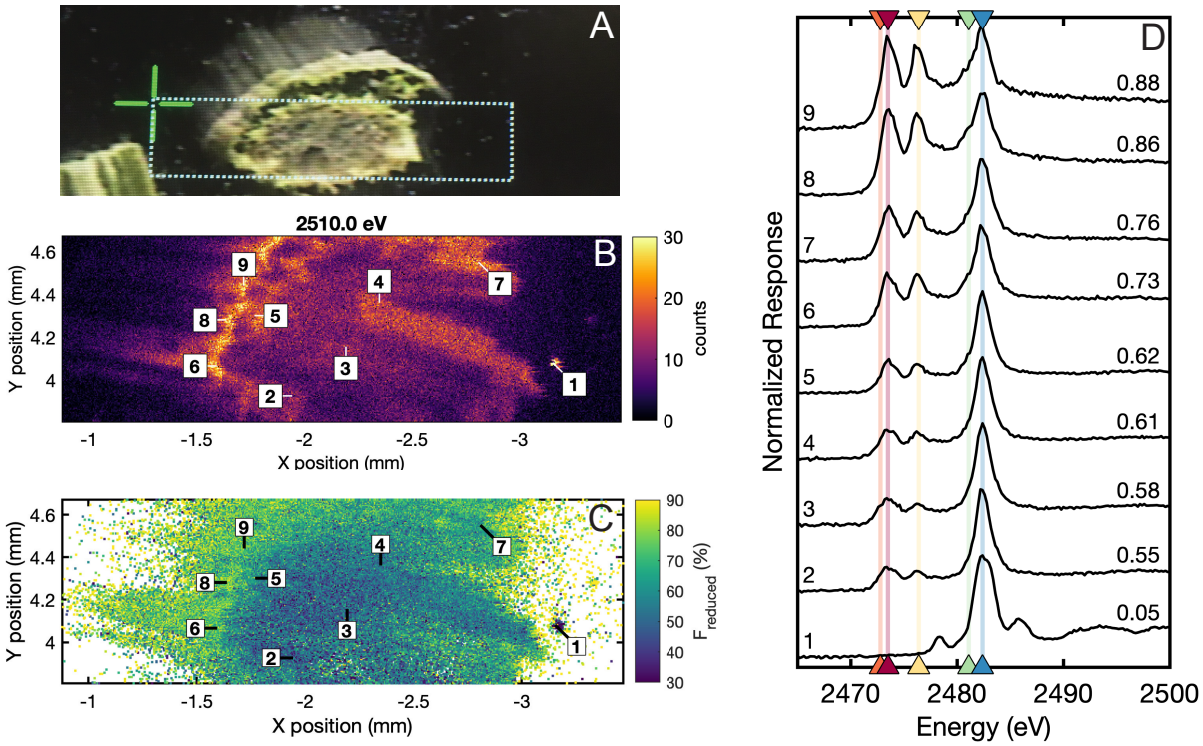

Fig. C.1. (A) Photograph of LHVS19-01 cross section, with dotted box indicating the approximate region of synchrotron analysis. (B) Fluorescence response at an incident energy of 2510.0 eV. This incident energy is above the sulfur K-edge and the response qualitatively reflected the abundance of S at each pixel. Cells along the outer surface of the cross section were enriched in S relative to those inside. (C) Pixel-by-pixel fitting of multiple energy maps to reference spectra from the ID 21 database of the European Synchrotron Radiation Facility. Each pixel indicates the value of $F_{reduced}$, which is the sum of fractional contributions from disulfide, thiol, and sulfoxide relative to the sum of all fractional contributions. Sulfur along the outer surface of the sample was reduced relative to sulfur inside. (D) X-ray absorption spectra collected at the indicated points of (B) and (C) identified a variety of reduced and oxidized S moieties. The numbers on the right of each spectra are $F_{reduced}$ values. Lines indicate characteristic locations for fluorescence peaks corresponding to disulfide (orange), thiol (red), sulfoxide (yellow), sulfonate (green), and sulfate (blue).

Appendix D. Seasonality of precipitation

Two meteorological stations near the Efri Haukadalsá catchment, the Ásgarður station and the Stykkishólm station, have historical data that partially constrained meteoric inputs into the catchment (Figs. 2, D.1). In the historical data both stations typically recorded less precipitation during the summer months than during the winter months (Fig. D.1A), and both the Ásgarður and Stykkishólm stations also showed summer declines in wind speed (Fig. D.1B).

Data collected further from the Efri Haukadalsá catchment constrained seasonal changes in precipitation chemistry (Fig. D.2). Two meteorological stations contributed data on precipitation chemistry as part of the European Monitoring and Evaluation Programme under the Convention on Long-Range Transboundary Air Pollution. A station at Íráfoss (code: IS0002R) has been operational since 1980, and a station at Stórhöfði (code: IS0091R) has been operational since 1995 (Fig. 2). Íráfoss is inland, while the Stórhöfði station is on an island off the southern coast of Iceland. The amount of precipitation at Íráfoss exhibited a summer reduction, analogous to Ásgarður and Stykkishólmur, while the amount of precipitation at Stórhöfði did not (Figs. D.2A, D.2B). During the winter months Cl^-/SO_4^{2-}, Cl^-/Ca^{2+}, Cl^-/Na^+, and Cl^-/Mg^{2+} at both the Íráfoss and Stórhöfði meteorological stations resembled marine ratios (Figs. D.2C- D.2F). During the summer months, the Cl^-/SO_4^{2-} and Cl^-/Ca^{2+} of precipitation at Íráfoss declined substantially (Figs. D.2C, D.2D, orange curves), while the Cl^-/Na^+ and Cl^-/Mg^{2+} ratios stayed near seawater values.

Values of Cl^-/SO_4^{2-} for summer precipitation, winter precipitation, and annually-integrated precipitation were calculated from measurements of dissolved chemistry reported at Íráfoss (Figs. 2, D.2, D.3). However, our major ion determinations in summer precipitation samples collected

near the Efri Haukadalsá catchment indicated a lower Cl^-/SO_4^{2-} ratio than calculated from the summer data at Íráfoss. We thus considered two possible end-members for annually-integrated precipitation, the first based on direct observations from Íráfoss and the second based on our observations in precipitation samples collected near the Efri Haukadalsá catchment. In either case, we used the mean $\delta^{34}S_{SO4}$ measured in our precipitation samples as the $^{34}S/^{32}S$ ratio of summer precipitation. Motivated by the observation that the major ion chemistry of winter precipitation from both Íráfoss and Stórhöfði resembled seawater (Fig. D.2), we assumed the $\delta^{34}S_{SO4}$ of winter precipitation equaled the marine value of 21‰. The fractional contribution of summer precipitation to annually-integrated precipitation was then calculated using observations of precipitation intensity from the two meteorological stations close to the Efri Haukadalsá catchment: Ásgarður with 23.1% of annual precipitation in summer, and Stykkishólmur with 22.2% of annual precipitation in summer (Fig. 2). A summer contribution of 22.6% was thus used to estimate the $\delta^{34}S_{SO4}$, and Cl^-/SO_4^{2-} in one case, of annually-integrated precipitation. Notably, our calculated value for the $\delta^{34}S_{SO4}$ of annually-integrated precipitation was near the maximum value observed in samples from Langjökull (Gislason & Torssander, 2006).

We thus reached two possible end-members representing annually-integrated precipitation with the same $\delta^{34}S_{SO4}$ but different Cl^-/SO_4^{2-} ratios (Fig. D.3). In the first end-member, the Cl^-/SO_4^{2-} ratio was derived from direct observations of annual precipitation chemistry at Íráfoss. In the second, the Cl^-/SO_4^{2-} ratio of annual precipitation was calculated from mixing fractions based on precipitation amounts at Ásgarður and Stykkishólm, our samples of summer precipitation, and the winter precipitation chemistry at Íráfoss. The Cl^-/SO_4^{2-} of annual precipitation calculated from the second approach was lower than directly observed at Íráfoss. However, in both cases the majority

of river water samples were consistent with mixing between basalt and annually-integrated precipitation. Moreover, differences in the mixing lines due to the different precipitation end-members were somewhat subsumed within uncertainty in the Cl^-/SO_4^{2-} ratio of the basalt end-member. Because it is unlikely that our few observations of precipitation chemistry captured the integrated chemical composition of summer precipitation, our favored annually-integrated precipitation end-member was that derived using the annual Cl^-/SO_4^{2-} observations from Íráfoss.

Previously published observations from several rivers in SW Iceland showed a seasonal transition in Cl^-/SO_4^{2-} and $\delta^{34}S_{SO4}$ (Gislason & Torssander, 2006) (Fig. D.4). This shift may reflect a lowering of summertime precipitation Cl^-/SO_4^{2-} as seen in the precipitation data from Íráfoss. Furthermore, some rivers showed a corresponding decline in $\delta^{34}S_{SO4}$ with decreasing Cl^-/SO_4^{2-}, suggesting that the $\delta^{34}S_{SO4}$ of summer precipitation was lower than the $\delta^{34}S_{SO4}$ of winter precipitation (Fig. D.4).

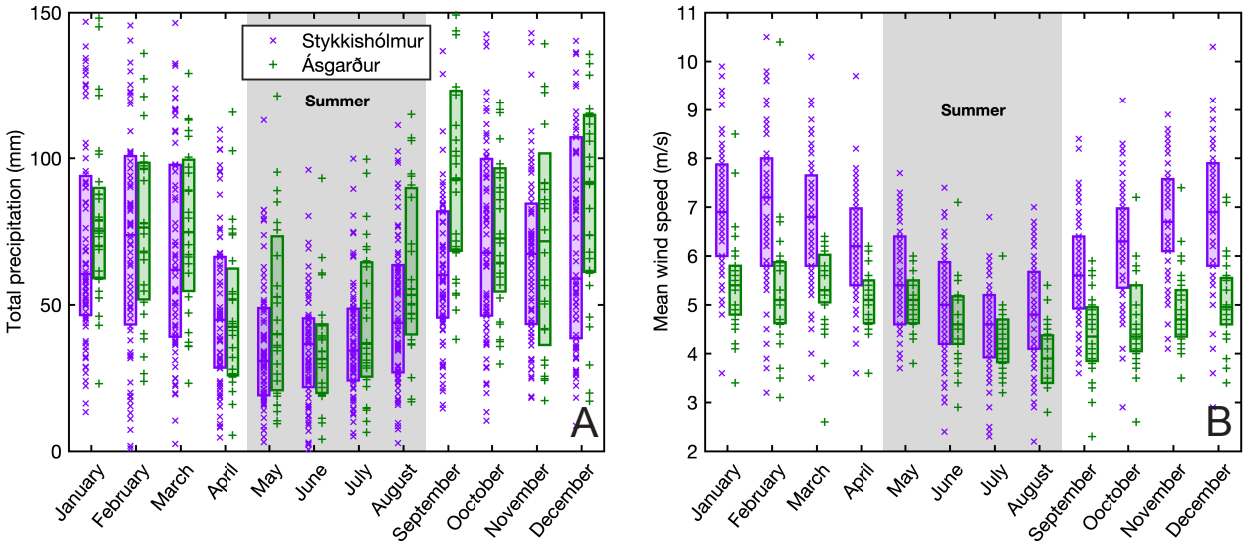

Fig. D.1. (A) Seasonal changes in the amount of precipitation and (B) wind speed at the Ásgarður and Stykkishólmur meteorological stations. Shaded boxes extend from the 25th to the 75th percentile of observed values for each month. At both stations precipitation and wind speed were lower during the summer season than during the rest of the year. The locations of the Ásgarður and Stykkishólmur meteorological stations are indicated in Fig. 2B of the main text.

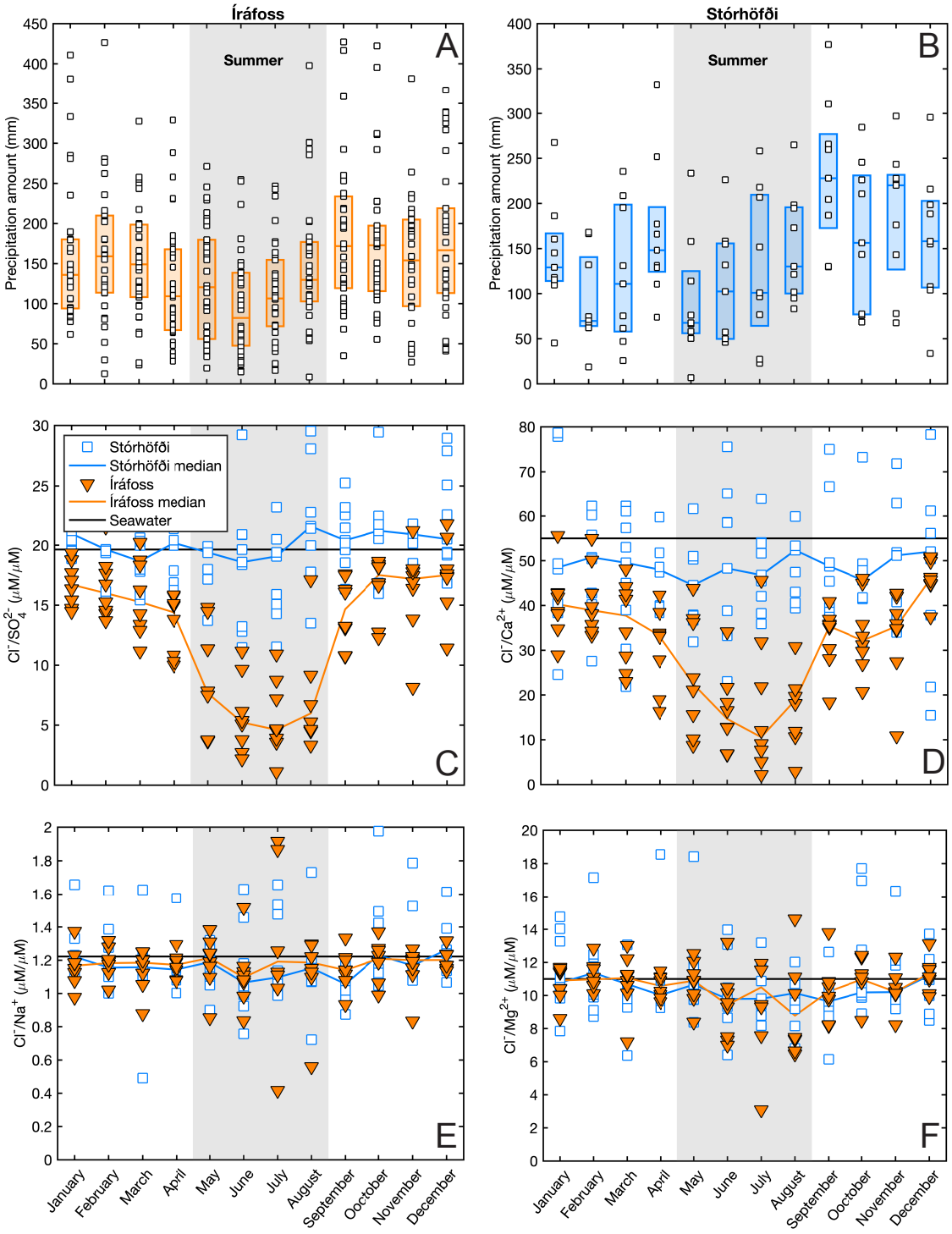

Fig. D.2. Seasonal changes in the (A, B) amount of precipitation and (C, D, E, F) ion chemistry at Íráfoss from 2006-2016 and Stórhöfði from 2002-2015. (A) There was generally less precipitation at Íráfoss during summer months than winter months, while (B) precipitation at Stórhöfði did not show clear seasonal behavior. (C) Cl^-/SO_4^{2-} and (D) Cl^-/Ca^{2+} were lower at Íráfoss during the summer months, while at Stórhöfði both ratios were relatively constant near seawater values. (E) Cl^-/Na^+ and (F) Cl^-/Mg^{2+} were constant near seawater values throughout the year at both Íráfoss and Stórhöfði. The location of the Íráfoss station is indicated in Fig. 2A of the main text.

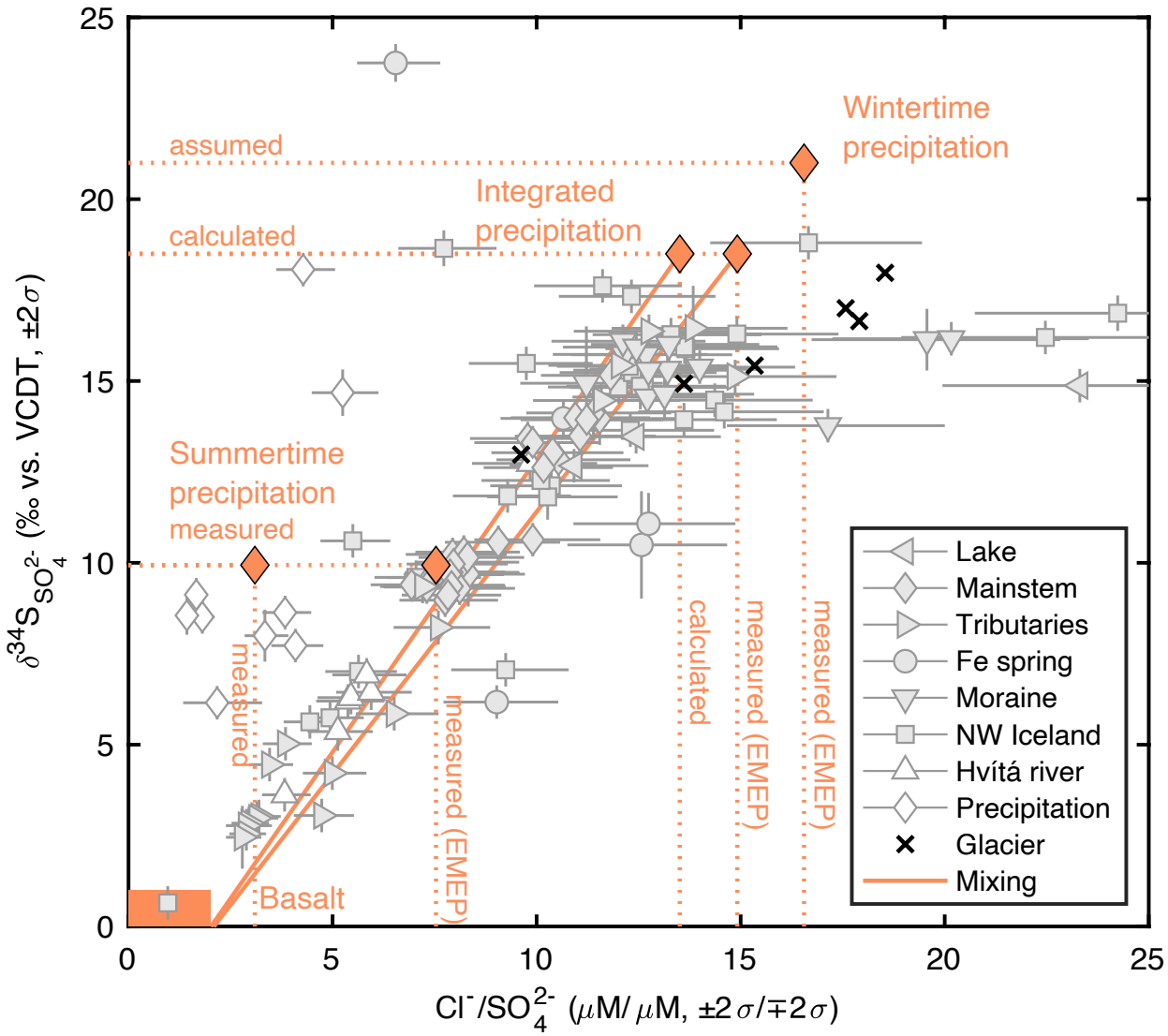

Fig. D.3. Sulfur isotope mixing diagram. River $\delta^{34}S_{SO4}$ against Cl^-/SO_4^{2-} with precipitation and basalt end-members. Note that two possible chemical compositions are plotted for summer precipitation and annually-integrated precipitation. Clay and carbonate end-members are not plotted because they do not contain SO_4^{2-} (Table E.1). EMEP refers to data from Íráfoss measured as part of European Monitoring and Evaluation Programme.

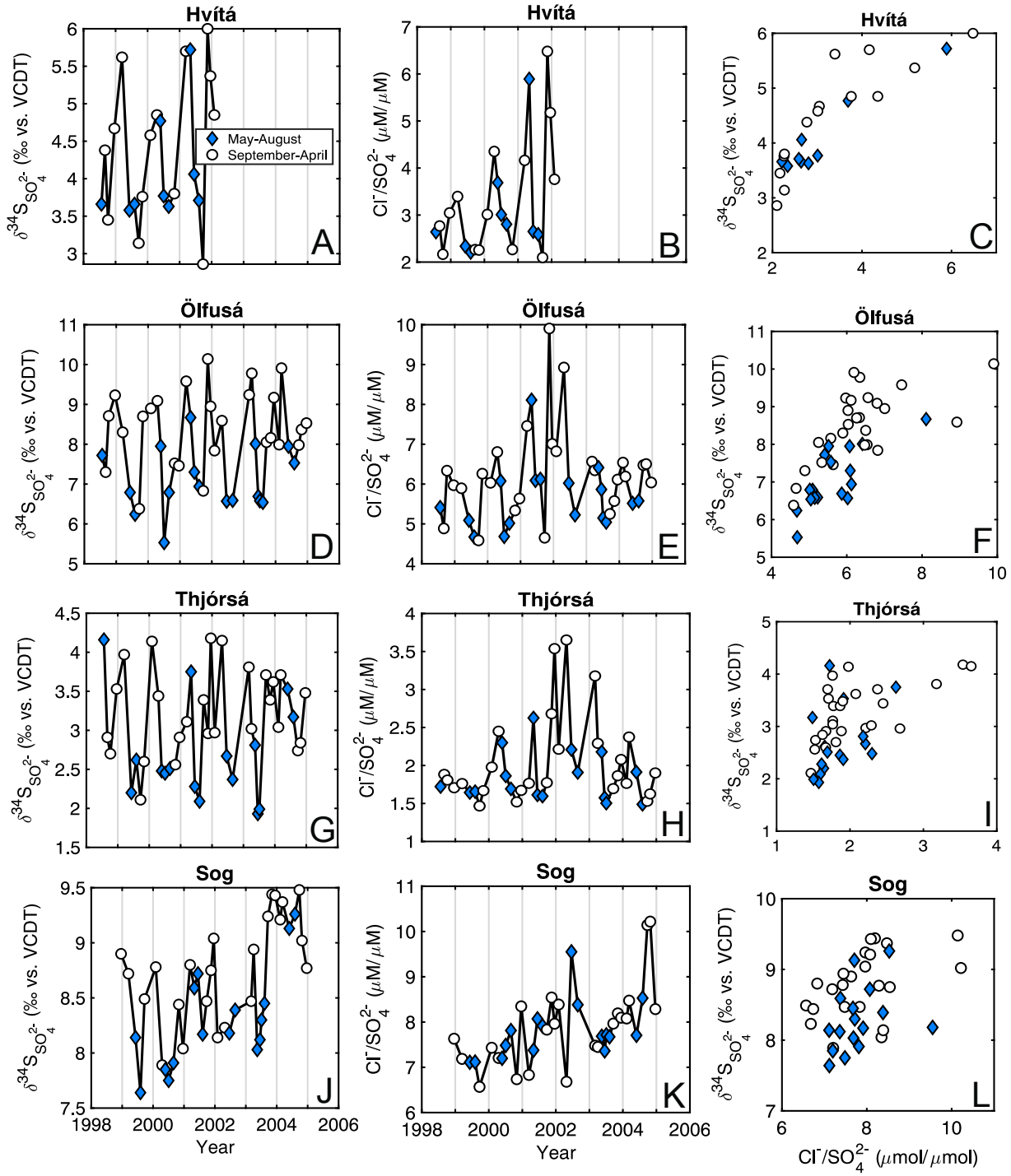

Fig. D.4. Seasonal changes in $\delta^{34}S_{SO4}$ and Cl^-/SO_4^{2-} of four rivers in Iceland. (A, B, C) The Hvítá River, (D, E, F) the Ölfusá River, (G, H, I) the Thjórsá River, and (J, K, L) the Sog river. Overall, river $\delta^{34}S_{SO4}$ and Cl^-/SO_4^{2-} appear lower during the summer months (blue diamonds) than during the remainder of the year (white circles). These data were consistent with summer changes in precipitation to lower $\delta^{34}S_{SO4}$ and Cl^-/SO_4^{2-} values. All measurements are from Gislason & Torssander (2006), replotted here.

Appendix E. River inversion model with Monte Carlo error propagation

Measured $[Ca^{2+}]$, $[Mg^{2+}]$, $[Na^{+}]$, $[K^{+}]$, $[Cl^{-}]$, $[SO_4^{2-}]$, and $\delta^{34}S_{SO4}$ were inverted using a mixing model with Monte Carlo error propagation to calculate the fractional contributions from summer precipitation, winter precipitation, basalt weathering, formation of secondary clays, and carbonate weathering (Table E.1) (Gaillardet et al., 1999). The chemical composition of Icelandic basalts was based on values reported in Torssander (1989), Gislason et al. (1996), and Moulton et al. (2000), the chemistry of clays was after Thorpe et al. (2019), and the carbonate end-member was assumed to be stoichiometric calcite (Table E.1). The chemistry of summer precipitation was based either on our precipitation samples from near the Efri Haukadalsá or on data from the Íráfoss meteorological station (Fig. D.3), and the chemistry of winter precipitation was calculated using observations from the Íráfoss meteorological station.

Dissolved chemistry was normalized to the charge-equivalent sum of cations ($\Sigma^{+} = 2*Ca^{2+} + 2*Mg^{2+} + Na^{+} + K^{+}$) (Torres et al., 2016; Kemeny et al., 2020). On each iteration, the values of Ca^{2+}/Σ^{+}, Mg^{2+}/Σ^{+}, Na^{+}/Σ^{+}, K^{+}/Σ^{+}, Cl^{-}/Σ^{+}, SO_4^{2-}/Σ^{+}, and $\delta^{34}S_{SO4}$ were pulled from normal distributions with predefined means and standard deviations. One cation ratio for each end-member was calculated by mass balance to ensure internal consistency, and the entire set of compositions was regenerated if any end-member ratios were negative. Moreover, on each iteration the dissolved chemistry of river samples was altered by values pulled from a distribution with mean of zero and a standard deviation corresponding to analytical precision. Each simulation optimized a cost function for misfit between observations and model results, using proportional misfit for concentration ratios and absolute misfit for $\delta^{34}S_{SO4}$. The fractional contribution of the clay end-member was constrained to be negative and contributions from all other end-members

were constrained to be positive. Solutions were only accepted if each dissolved concentration was reconstructed within 25% and the value of $\delta^{34}S_{SO4}$ was reconstructed within 2‰. The river inversion model was run with and without the carbonate end-member and for two different summer precipitation end-members (Table E.1).

Prior observations have demonstrated that secondary clay formation occurs throughout Icelandic catchments, with evidence from dissolved major ion concentrations, isotopic ratios, and the chemistry of soils (Gislason et al., 1996; Moulton et al., 2000; Stefánsson & Gislason, 2001; von Strandmann et al., 2006, 2012; Georg et al., 2007; Vigier et al., 2009; Pearce et al., 2010; Hindshaw et al., 2013; Opfergelt et al., 2017). Consistent with this prior work, our inversion model constrained the median consumption of cations by clay formation to be 3-6% of Σ^+ in samples from the Efri Haukadalsá and 15-18% of Σ^+ in samples from the Hvítá catchment (Fig. E.1). Our results were thus consistent with Hindshaw et al. (2013), who interpreted Ca^{2+} isotope ratios as showing enhanced clay formation in currently glaciated catchments relative to catchments without glaciers. The fractional uptake of cations by clay and the inversion-constrained chemical composition of the clay end-member only changed minimally when also including a calcite end-member in the inversion, as suggested by some interpretations of Ca^{2+} and Sr^{2+} isotope data (Jacobson et al., 2015; Andrews & Jacobson, 2017) (Fig. E.2). Notably, these results were not meant to fully constrain the nature of clay formation or carbonate weathering in the Efri Haukadalsá catchment, but simply to demonstrate that our interpretation of measured $\delta^{34}S_{SO4}$ values was consistent with the broader understanding of active weathering processes in Iceland.

Table E.1: End-member values and distributions for Monte Carlo inversion model. Values for integrated precipitation (final two rows of the table) are not used in the Monte Carlo inversion model but are provided here as the $\delta^{34}S_{SO4}$ and Cl^-/SO_4^{2-} ratios are used in the Rayleigh model calculations described below (Appendix J). The chemistry of basalt was calculated from measurements presented in Torssander (1989), Gislason et al. (1996), and Moulton et al. (2000), the chemistry of summertime and wintertime precipitation was calculated from precipitation samples collected near the Efri Haukadalsá and measurements reported as part of the European Monitoring and Evaluation Programme, and the chemistry of clays was calculated using measurements from Thorpe et al. (2019). The chemistry of the carbonate end-member was a stoichiometric calcite.

End-Member	$\mathbf{Ca^{2+}/\Sigma^+}$	$\mathbf{Mg^{2+}/\Sigma^+}$	$\mathbf{Na^+/\Sigma^+}$	$\mathbf{K^+/\Sigma^+}$	$\mathbf{Cl^-/\Sigma^+}$	$\mathbf{SO_4^{2-}/\Sigma^+}$	$\mathbf{Cl^-/SO_4^{2-}}$	$\mathbf{\delta^{34}S_{SO4}}$
Basalt	0.48 ± 0.06	0.39 ± 0.11	0.12 ± 0.07	0.01 ± 0.02	0.00 ± 0.00	0.00 - 0.25	0	-2.0 - 2.5
Summer prec. (Íráfoss)	0.09 ± 0.06	0.16 ± 0.03	0.69 ± 0.09	0.06 ± 0.06	0.91 ± 0.30	0.24 ± 0.12	7.5	9.9 ± 3.8
Summer prec. (Efri Haukadalsá)	0.34 ± 0.21	0.09 ± 0.04	0.47 ± 0.18	0.09 ± 0.04	0.49 ± 0.16	0.34 ± 0.20	3.1	9.9 ± 3.8
Winter prec.	0.05 ± 0.02	0.17 ± 0.02	0.76 ± 0.03	0.03 ± 0.01	0.88 ± 0.12	0.11 ± 0.02	16.6	21 ± 0.5
Clay	0.37 ± 0.10	0.42 ± 0.07	0.07 ± 0.04	0.14 ± 0.05	0.00 ± 0.00	0.00 ± 0.00	-	-
Carbonate	1.00 ± 0.00	0.00 ± 0.00	0.00 ± 0.00	0.00 ± 0.00	0.00 ± 0.00	0.00 ± 0.00	-	-
Integrated prec. (Íráfoss)	0.05 ± 0.05	0.17 ± 0.02	0.75 ± 0.07	0.03 ± 0.04	0.88 ± 0.55	0.12 ± 0.11	14.9	18.5
Integrated prec. (Efri Haukadalsá)	-	-	-	-	-	-	13.5	18.5

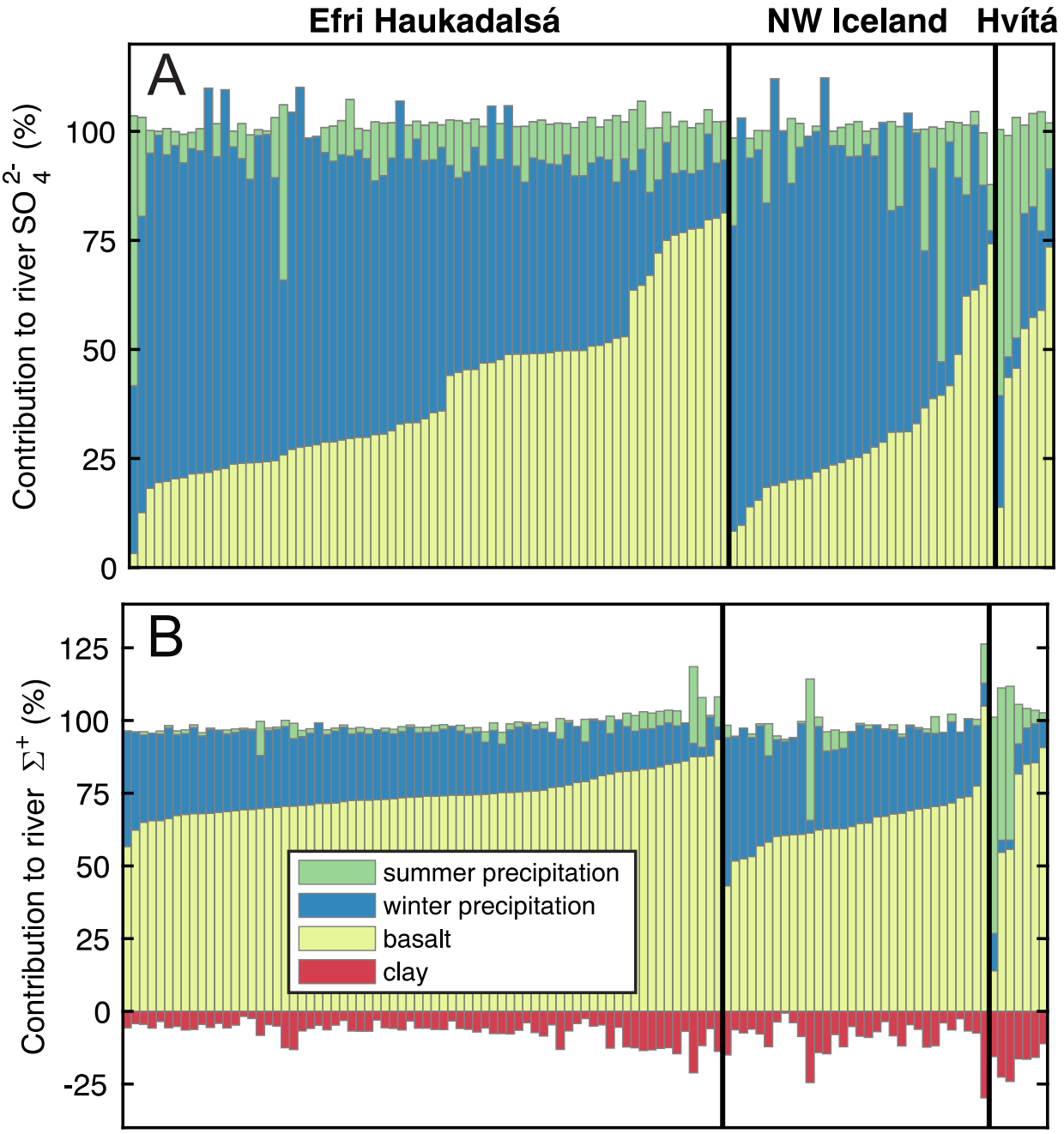

Fig. E.1. Inversion results for the fractional contributions of summer precipitation, winter precipitation, basalt weathering, and clay formation to measured (A) [SO_4^{2-}] and (B) [Σ^+]. The clay end-member plots as a negative contribution to [Σ^+] because it removes cations from solution and does not contribute to [SO_4^{2-}] because it does not contain SO_4^{2-} (Table E.1). Results are for an inversion where summer precipitation Cl^-/SO_4^{2-} reflects measurements in samples collected near the Efri Haukadalsá catchment.

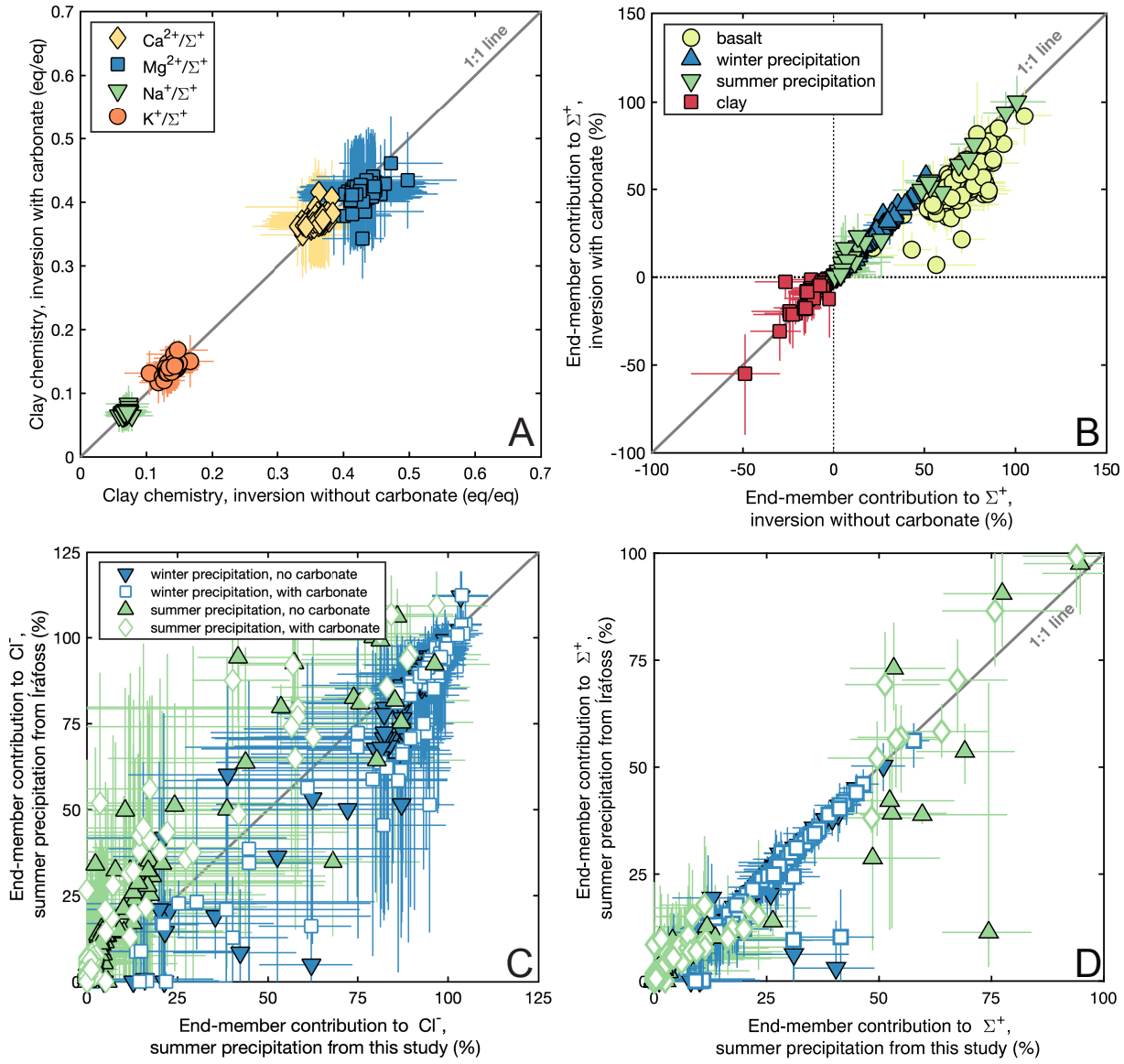

Fig. E.2. Results of inversion models with Monte Carlo error propagation. (A) Comparison of Mg^{2+}/Σ^+, Ca^{2+}/Σ^+, Na^+/Σ^+, and K^+/Σ^+ of the clay end-member in calculations with and without a carbonate end-member. The inversion-constrained chemistry of the clay end-member was similar in the two cases, although shifted to slightly higher Ca^{2+}/Σ^+ and slightly lower Mg^{2+}/Σ^+ when carbonate was included in the inversion. (B) Contribution of basalt, clay, summer precipitation, and winter precipitation to Σ^+ in inversions with and without a carbonate end-member. The inversion results were again similar for the two cases. (C) The fractional contribution of summer (green symbols) and winter precipitation (blue symbols) to river $[Cl^-]$ or (D) $[\Sigma^+]$ in inversions with (open symbols) and without (closed symbols) a carbonate end-member when summer precipitation was either our observations in samples collected near the Efri Haukadalsá or observations from the Íráfoss meteorological station. The choice of precipitation end-member mostly had a minimal impact on results, but did substantially change the fractional contribution of summertime precipitation for several samples. Error bars in all panels range from the 25th to 75th percentile of accepted inversion results.

Appendix F. Extended geomorphic analysis

We conducted three analyses to quantitatively relate the topographic structure of the Efri Haukadalsá catchment with river chemistry. The first and third analyses are presented in the main text (Fig. 8), and results for the second analysis are below (Fig. F.1). We compared $\delta^{34}S_{SO4}$ to the mean power law exponent *b* for cross sections upstream of each sample site and found that lower $\delta^{34}S_{SO4}$ values are associated with V-shaped profiles (Fig. F.1A, B). The mean power law exponent upstream of each sample were similar for the two quantitative analyses (Fig. F.1C).

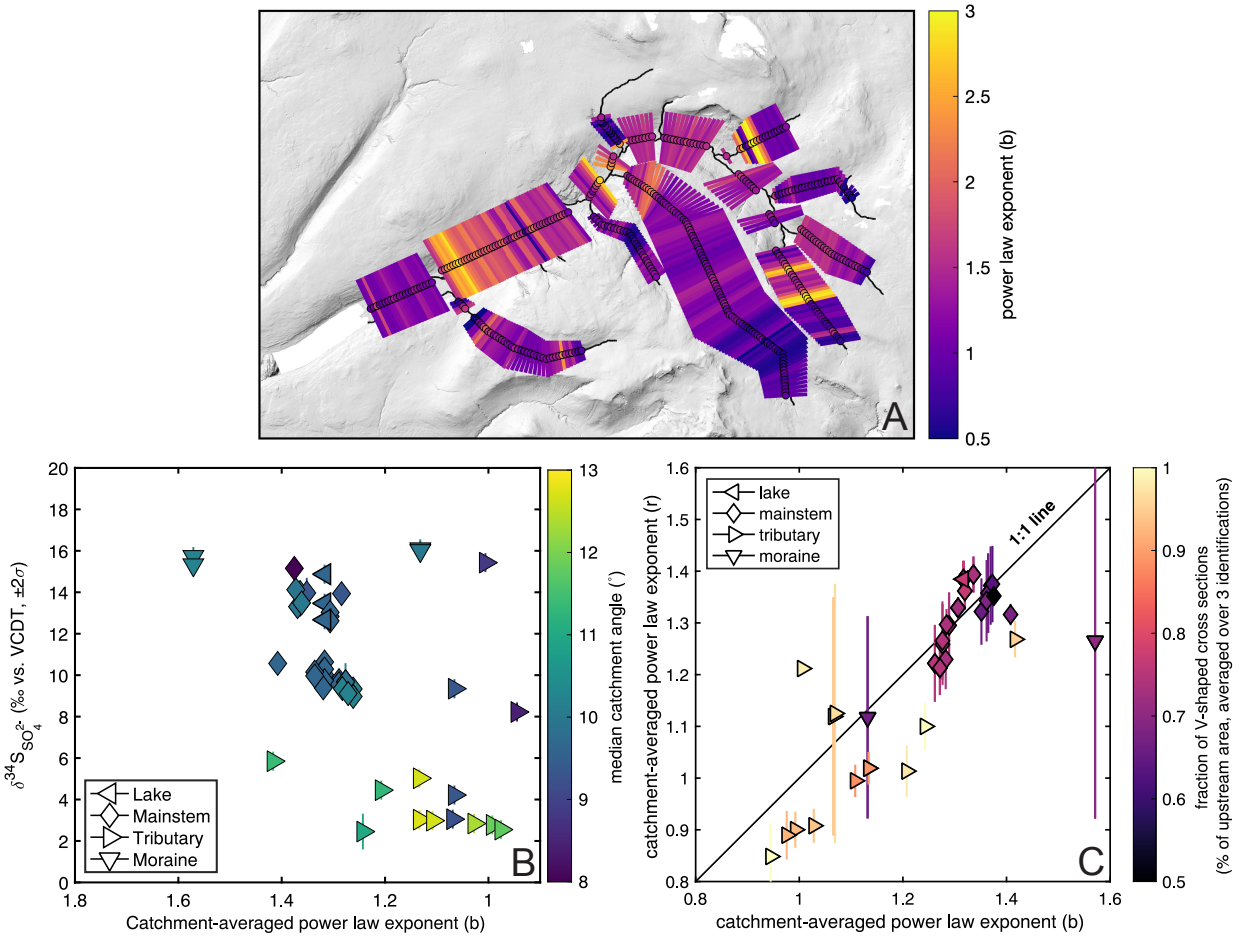

Fig. F.1: Results of quantitative cross section fitting. To calculate the mean power law exponent (*b*), each cross section was split at a center point and the two sides were independently fit to power law functions. (A) Map of *b* for each profile. (B) Values of $\delta^{34}S_{SO4}$ against the mean *b* upstream of each sampling site. Lower values of $\delta^{34}S_{SO4}$ were associated with V-shaped cross sections. (C) Comparison of the power law exponent calculated as the mean of the two-sided fits (*b*) against the single power-law exponent fit (*r*) after Allen et al. (2018) coded by the fraction of upstream V-shaped cross section identified manually. The three approaches were largely in mutual agreement.

Appendix G. Additional maps of dissolved chemistry

Our analysis identified spatial gradients in the $\delta^{34}S_{SO4}$ and $[SO_4^{2-}]$ values of river water samples in the Efri Haukadalsá catchment (Fig. 7). Maps for $[Ca^{2+}]$, $[Mg^{2+}]$, $[Na^{+}]$, $[K^{+}]$, $[Cl^{-}]$ and the sum of cations $[\Sigma^{+}]$ are below (Fig. G.1).

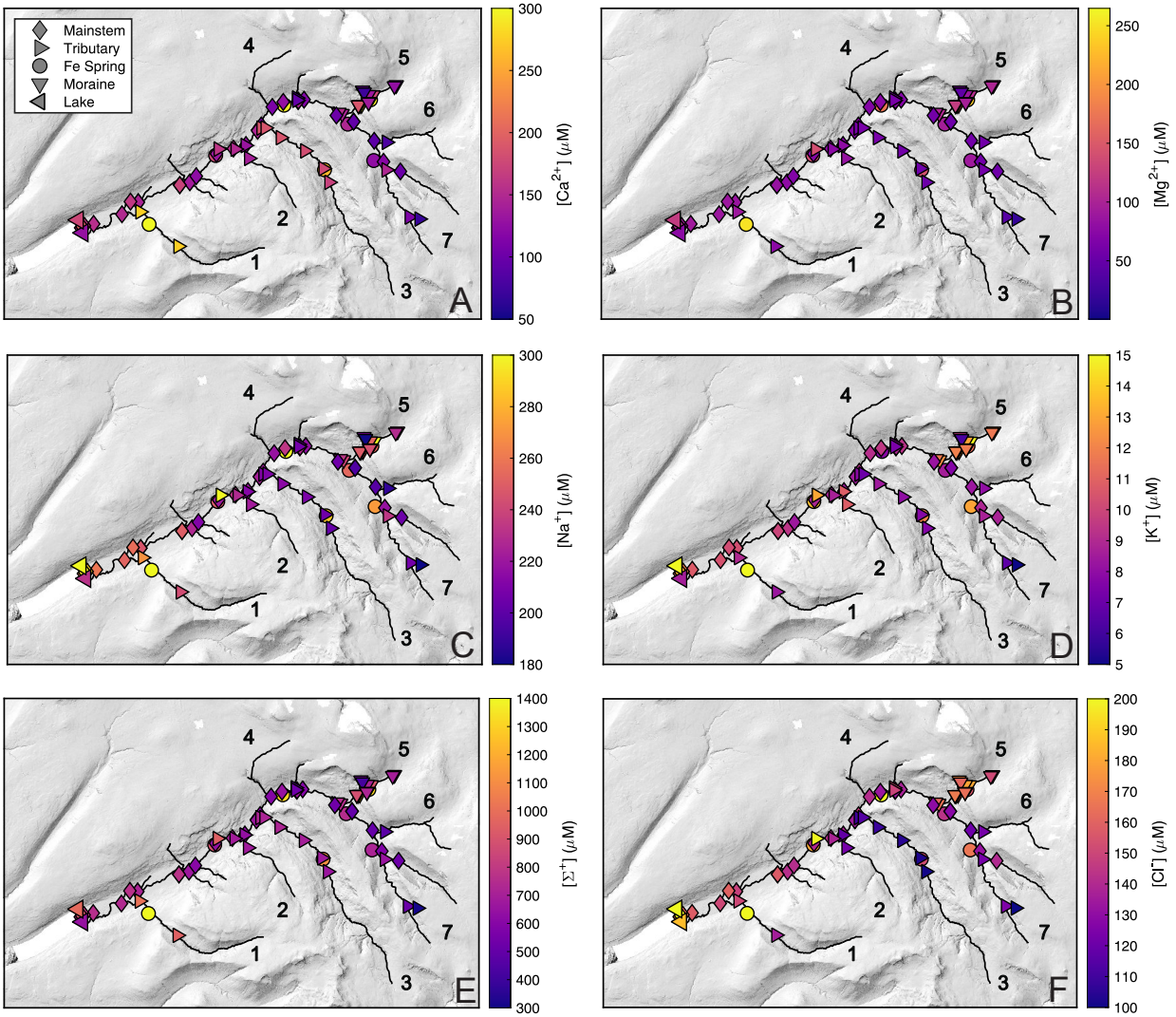

Fig. G.1. Dissolved chemistry of river water samples collected throughout the Efri Haukadalsá. (A) $[Ca^{2+}]$, (B) $[Mg^{2+}]$, (C) $[Na^{+}]$, (D) $[K^{+}]$, (E) $[\Sigma^{+}]$, and (F) $[Cl^{-}]$.

Appendix H. Chemostatis in the Efri Haukadalsá

River water samples in this study that were collected close in space were also often collected close in time, meaning that it is formally possible that our observations of spatial structure in dissolved chemistry reflected sampling bias. That is, if the Efri Haukadalsá had a uniform isotopic composition that changed on a timescale of hours to days, our sampling could theoretically have reflected whole-river changes in isotopic composition rather than strong morphologic control on $\delta^{34}S_{SO4}$. We rejected this possibility on the basis of two experiments: sampling many locations along the Efri Haukadalsá within a single day and sampling the same locations at multiple times.

On July 30th, 2019 we collected 21 river water samples along the lower and middle reaches of the Efri Haukadalsá (Fig. H.1). The $\delta^{34}S_{SO4}$ of these samples ranged from 3.0‰ to 16.0‰ and reflected the same isotopic structure seen in our full sample suite. Samples from tributary 1 and tributary 3 had low $\delta^{34}S_{SO4}$ values, the river near the moraine had high $\delta^{34}S_{SO4}$ values, and the lower valley had intermediate $\delta^{34}S_{SO4}$ values. Moreover, locations sampled multiple times over a single field season or across field seasons retained their chemical characteristics. For example, river water samples LHWS19-04 and LHWS19-25 were collected from the same location in the Efri Haukadalsá on July 28th and July 30th of 2019, respectively. These samples had extremely similar [SO_4^{2-}] values of 12.2 μM and 12.9 μM, as well as indistinguishable $\delta^{34}S_{SO4}$ values of 12.8‰ and 12.6‰, respectively. Samples collected in 2016 and 2019 from either a tributary (LHWS16-11, LHWS19-03) or the Efri Haukadalsá mainstem (LHWS16-08d, LHWS19-9) were also similar despite the three years separating sample collection (Table H.1). These data showed that the Efri Haukadalsá was not isotopically uniform at any instant, that chemical gradients were sustained through time, and that our observation of spatial structure in $\delta^{34}S_{SO4}$ was not a sampling artifact.

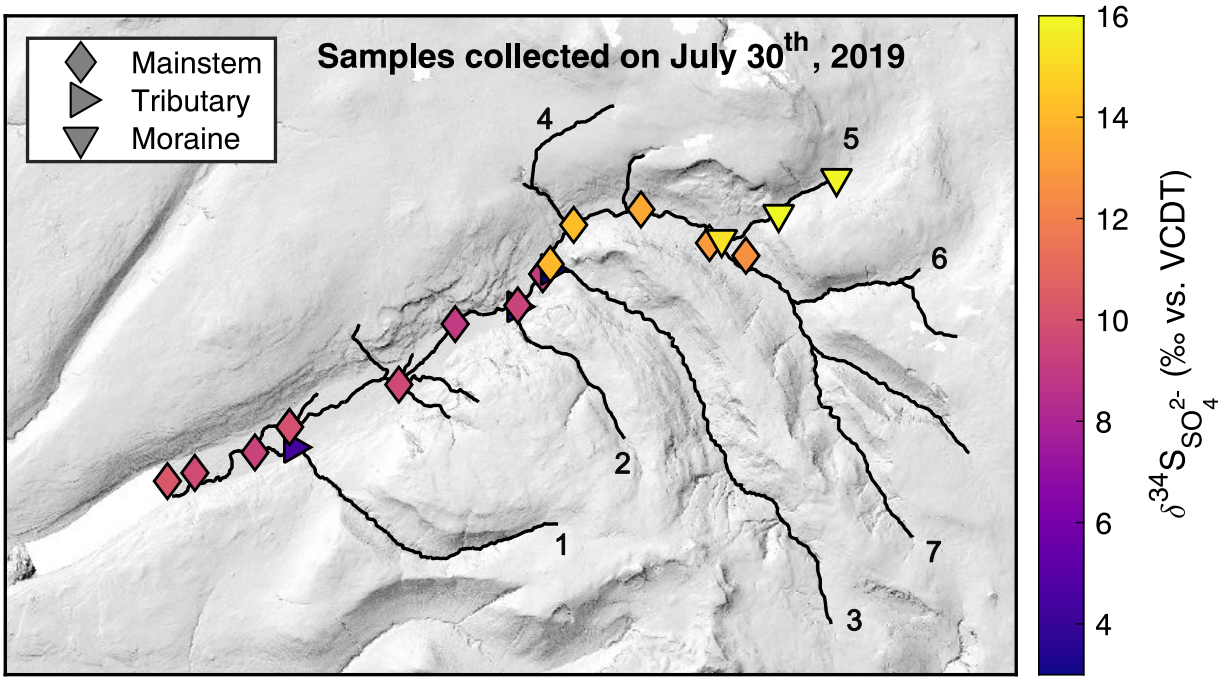

Fig. H.1. Values of river water $\delta^{34}S_{SO4}$ in samples collected on a single day throughout the Efri Haukadalsá catchment. Consistent with our full sample suite, values of $\delta^{34}S_{SO4}$ were low in tributaries 1, 2, and 3, elevated in the upper valley and tributary 5, and intermediate in the lower valley. These results led us to conclude that the observed patterns in $[SO_4^{2-}]$ and $\delta^{34}S_{SO4}$ did not reflect whole-river changes giving the appearance of spatial organization due to sampling artifacts.

Table H.1: Dissolved chemistry (mean ± 2σ) of samples collected from approximately the same locations within one field season (LHWS19-04 and LHWS19-25) or in two different field seasons (LHWS16-11 and LHWS19-03, LHWS16-08d and LHWS19-19). In the latter two examples, the chemistry of samples is extremely consistent despite the three years separating collection. These paired samples represent three different locations within the catchment of the Efri Haukadalsá.

Sample	$\delta^{34}S_{SO4}$	$[SO_4^{2-}]$	$[Cl^-]$	$[Ca^{2+}]$	$[Mg^{2+}]$	$[Na^+]$	$[K^+]$
LHWS19-04	12.8±0.5	12.2±0.9	128.4±10.6	95.3±12.8	55.8±3.9	196.3±7.3	7.7±0.6
LHWS19-25	12.6±0.5	12.9±0.9	130.9±10.8	97.8±13.2	57.0±4.0	202.8±7.6	8.2±0.6
LHWS16-11	16.4±0.5	11.7±0.9	149.5±12.3	96.7±13.0	64.1±4.5	207.0±7.7	7.4±0.6
LHWS19-03	16.4±1.2	11.1±0.8	153.3±12.6	83.3±11.2	63.4±4.5	206.1±7.7	8.0±0.6
LHWS16-08d	9.4±0.5	19.4±1.4	134.5±11.1	146.2±19.7	71.6±5.1	223.9±8.3	8.5±0.7
LHWS19-19	9.1±0.5	17.6±1.3	137.5±11.3	132.2±17.8	70.3±5.0	219.9±8.2	8.8±0.7

Appendix I. Temporal changes in Haukadalsvatn chemistry

We collected one sample of lake water from Haukadalsvatn in 2016 and another in 2019. The two samples had relatively similar [SO_4^{2-}] values, 14.6 μM and 17.0 μM, and similar $\delta^{34}S_{SO4}$ values of 14.9‰ and 12.7‰. However, the value of [Cl^-] in the two samples was quite different, with the 2016 sample having 340 μM and the 2019 sample having 186 μM, resulting in Cl^-/SO_4^{2-} values of 23.3 and 10.9, respectively. The 2016 sample was also enriched by a factor of 1.4 to 1.7 in the values of [Ca^{2+}], [Mg^{2+}], [Na^+], and [K^+] relative to the 2019 sample. A 2016 sample collected near the lake outflow had chemical concentrations mostly intermediate between the two lake samples, although with higher [SO_4^{2-}]. Moreover, the 2016 and 2019 lake samples differed in [SO_4^{2-}] from a sample previously collected from Haukadalsvatn reported in Langdon et al. (2008).

The residence time of water in Haukadalsvatn is only approximately 2-3 months, as calculated using a discharge of 13.4 m^3/sec and depth estimates from the bathymetry map of Geirsdóttir et al. (2009). Such a short residence time indicated that observed chemical changes could reflect short-term changes in lacustrine dynamics. However, the observed chemical differences may also be attributable to sampling location; the 2016 sample was collected from the lake shore in extremely shallow water, while the more dilute 2019 sample was collected while standing in the lake approximately 10 meters from shore in >1 m water depth. The differences between the 2016 and 2019 samples could thus reflect either terrestrial runoff or inputs from shallow sediment to the perimeter of the lake.

Appendix J. Rayleigh model for sediment $\delta^{34}S$

We modeled the Cl^-/SO_4^{2-} and $\delta^{34}S_{SO4}$ values of river water samples as reflecting the mixing of basalt and annually-integrated precipitation (eqs. J.1, J.2) followed by closed-system fractionation (eq. J.3). Our model had two measured parameters, Cl^-/SO_4^{2-} and $\delta^{34}S_{SO4}$, and three unknowns: the basalt mixing fraction (f_{mix}), the fraction of SO_4^{2-} remaining ($f_{remaining}$), and the isotope effect of the SO_4^{2-}-consuming process ($^{34}\alpha$). As described in the main text, we estimated that no more than 10% of the initial SO_4^{2-} budget was likely reduced to S_{org}, and thus constrained the model to have 90% of initial SO_4^{2-} remaining ($f_{remaining}$=90%; we used the range 85-95% as error bars on the calculation). We then optimized a cost function $\mathbf{c}\left(f_{mix}, {}^{34}\alpha\right)$ for the mixing fraction and isotope effect that minimized proportional misfit from observations (eq. J.4; Fig. J.1A, B) and solved for the $\delta^{34}S$ of sulfur that would be produced from the fractionating process (Fig. J.1E, F). The calculation found isotope effects lower in magnitude than commonly expected for MSR (Fig. J.1C, D). Moreover, the model predicted sediment $\delta^{34}S$ values lower than observed, leading us to conclude that observed S_{org} phases were not derived from microbial SO_4^{2-} reduction. Rather, we concluded that S_{org} likely formed from SO_4^{2-} assimilation and reduction within biomass.

$$^{34}R_{mix} = {}^{34}R_{VCDT}\left(f_{mix}\left(\frac{\delta^{34}S_{basalt}}{10^3}+1\right)+(1-f_{mix})\left(\frac{\delta^{34}S_{precipitation}}{10^3}+1\right)\right) \quad \text{(eq. J.1)}$$

$$\left(\frac{Cl^-}{SO_4^{2-}}\right)_{model} = \frac{\left(f_{mix}\left(\frac{Cl^-}{SO_4^{2-}}\right)_{basalt}+(1-f_{mix})\left(\frac{Cl^-}{SO_4^{2-}}\right)_{precipitation}\right)}{f_{remaining}} \quad \text{(eq. J.2)}$$

$$\delta^{34}S_{model} = \left(\frac{{}^{34}R_{mix}*\left(f_{remaining}\right)^{{}^{34}\alpha-1}}{{}^{34}R_{VCDT}}-1\right)10^3 \quad \text{(eq. J.3)}$$

$$\boldsymbol{c}\left(f_{mix}, {}^{34}\alpha\right) = \sqrt{\left(\frac{\delta^{34}S_{river}-\delta^{34}S_{model}}{\delta^{34}S_{river}}\right)^2+\left(\frac{\left(\frac{Cl^-}{SO_4^{2-}}\right)_{river}-\left(\frac{Cl^-}{SO_4^{2-}}\right)_{model}}{\left(\frac{Cl^-}{SO_4^{2-}}\right)_{river}}\right)^2} \quad \text{(eq. J.4)}$$

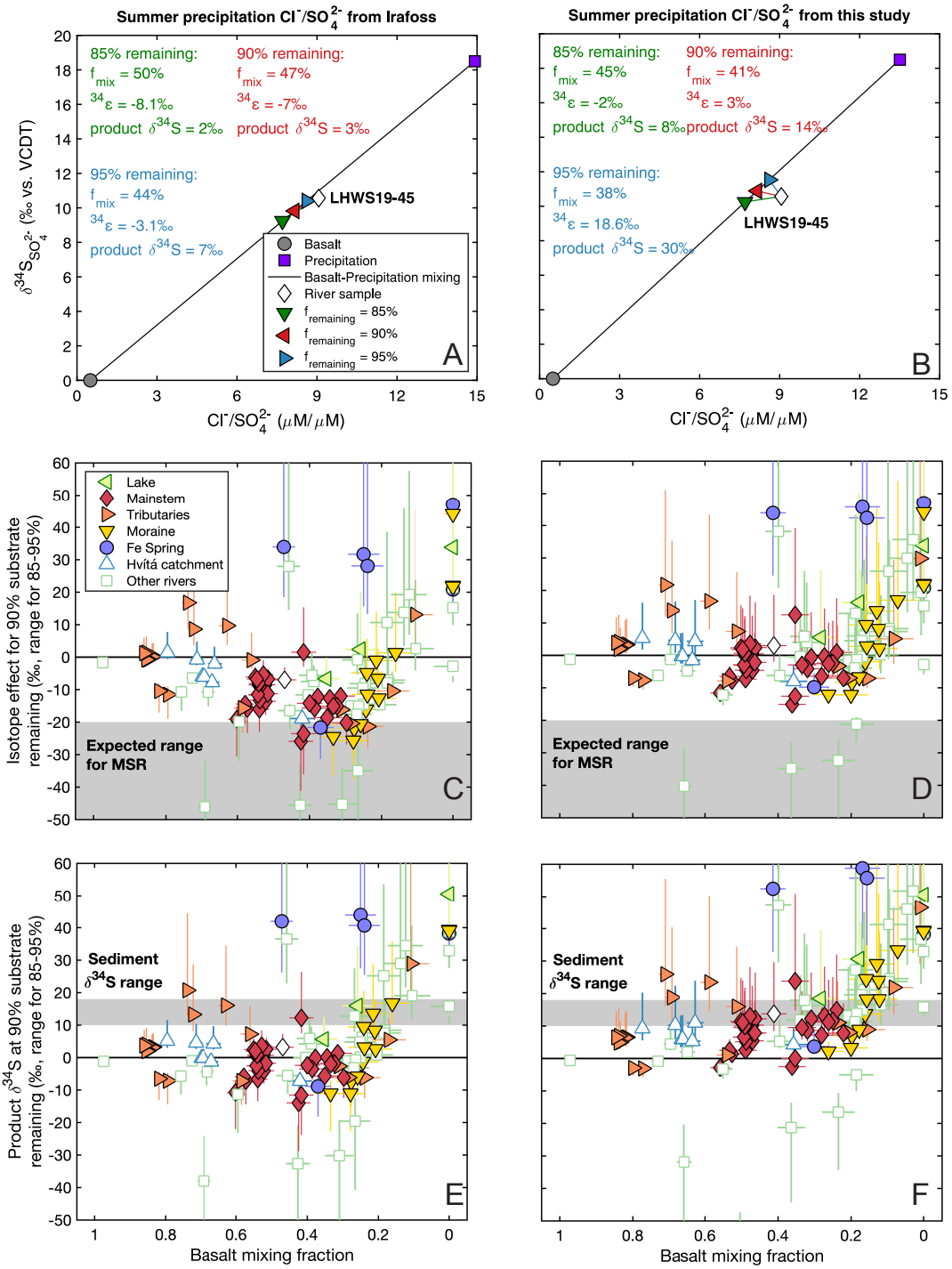

Fig. J.1. (A, B) Example of Rayleigh calculation for sample LHWS19-45. (C, D) The isotope effect and (E, F) integrated product $\delta^{34}S$ required to explain deviations from mixing of basalt and annually-integrated precipitation when 90% of SO_4^{2-} remains in solution (range is given for 85-95%). While the isotope effects were potentially consistent with MSR, the required $\delta^{34}S$ of the product was lower than measured sediment $\delta^{34}S$. Panels (A, C, E) show results when the annually-integrated precipitation end-member has Cl^-/SO_4^{2-} derived using data at Íráfoss, and panels (B, D, F) show results when the annually-integrated precipitation end-member has Cl^-/SO_4^{2-} derived from our samples of summer precipitation collected near the Efri Haukadalsá catchment.

References:

Allen, G. H., Pavelsky, T. M., Barefoot, E. A., Lamb, M. P., Butman, D., Tashie, A., & Gleason, C. J. (2018). Similarity of stream width distributions across headwater systems. *Nature communications*, 9(1), 1-7, https://doi.org/10.1038/s41467-018-02991-w.

Andrews, M. G., & Jacobson, A. D. (2017). The radiogenic and stable Sr isotope geochemistry of basalt weathering in Iceland: role of hydrothermal calcite and implications for long-term climate regulation. *Geochimica et Cosmochimica Acta*, 215, 247-262, https://doi.org/10.1016/j.gca.2017.08.012.

Gaillardet, J., Dupré, B., Louvat, P., & Allegre, C. J. (1999). Global silicate weathering and CO_2 consumption rates deduced from the chemistry of large rivers. *Chemical geology*, *159*(1), 3-30, https://doi.org/10.1016/S0009-2541(99)00031-5.

Georg, R. B., Reynolds, B. C., West, A. J., Burton, K. W., & Halliday, A. N. (2007). Silicon isotope variations accompanying basalt weathering in Iceland. *Earth and Planetary Science Letters*, 261(3-4), 476-490, https://doi.org/10.1016/j.epsl.2007.07.004.

Geirsdóttir, Á., Miller, G. H., Thordarson, T., & Ólafsdóttir, K. B. (2009). A 2000 year record of climate variations reconstructed from Haukadalsvatn, West Iceland. *Journal of Paleolimnology*, *41*(1), 95-115, https://doi.org/10.1007/s10933-008-9253-z.

Gislason, S. R., Arnorsson, S., & Armannsson, H. (1996). Chemical weathering of basalt in Southwest Iceland; effects of runoff, age of rocks and vegetative/glacial cover. *American Journal of Science*, 296(8), 837-907, https://doi.org/10.2475/ajs.296.8.837.

Gislason, S. R., & Torssander, P. (2006). Response of sulfate concentration and isotope composition in Icelandic rivers to the decline in global atmospheric SO_2 emissions into the North Atlantic region. *Environmental science & technology*, *40*(3), 680-686, https://doi.org/10.1021/es051325o.

Hindshaw, R. S., Bourdon, B., von Strandmann, P. A. P., Vigier, N., & Burton, K. W. (2013). The stable calcium isotopic composition of rivers draining basaltic catchments in Iceland. *Earth and Planetary Science Letters*, 374, 173-184, https://doi.org/10.1016/j.epsl.2013.05.038.

Jacobson, A. D., Andrews, M. G., Lehn, G. O., & Holmden, C. (2015). Silicate versus carbonate weathering in Iceland: New insights from Ca isotopes. *Earth and Planetary Science Letters*, *416*, 132-142, https://doi.org/10.1016/j.epsl.2015.01.030.

Kemeny, P. C., Lopez, G. I., Dalleska, N. F., Torres, M., Burke, A., Bhatt, M. P., ... & Adkins, J. F. Sulfate sulfur isotopes and major ion chemistry reveal that pyrite oxidation counteracts CO_2 drawdown from silicate weathering in the Langtang-Trisuli-Narayani River system, Nepal Himalaya. *Geochimica et Cosmochimica Acta*, 294, 43-69, https://doi.org/10.1016/j.gca.2020.11.009.

Langdon, P. G., Holmes, N., & Caseldine, C. J. (2008). Environmental controls on modern chironomid faunas from NW Iceland and implications for reconstructing climate change. *Journal of Paleolimnology*, 40(1), 273-293, https://doi.org/10.1007/s10933-007-9157-3.

Moulton, K. L., West, J., & Berner, R. A. (2000). Solute flux and mineral mass balance approaches to the quantification of plant effects on silicate weathering. *American Journal of Science*, 300(7), 539-570, https://doi.org/10.2475/ajs.300.7.539.

Opfergelt, S., Williams, H. M., Cornelis, J. T., Guicharnaud, R. A., Georg, R. B., Siebert, C., ... & Burton, K. W. (2017). Iron and silicon isotope behaviour accompanying weathering in

Icelandic soils, and the implications for iron export from peatlands. *Geochimica et Cosmochimica Acta*, 217, 273-291, https://doi.org/10.1016/j.gca.2017.08.033.

Pearce, C. R., Burton, K. W., von Strandmann, P. A. P., James, R. H., & Gíslason, S. R. (2010). Molybdenum isotope behaviour accompanying weathering and riverine transport in a basaltic terrain. *Earth and Planetary Science Letters*, 295(1-2), 104-114, https://doi.org/10.1016/j.epsl.2010.03.032.

Stefánsson, A., & Gislason, S. R. (2001). Chemical weathering of basalts, Southwest Iceland: effect of rock crystallinity and secondary minerals on chemical fluxes to the ocean. *American Journal of Science*, 301(6), 513-556, https://doi.org/10.2475/ajs.301.6.513.

Thorpe, M. T., Hurowitz, J. A., & Dehouck, E. (2019). Sediment geochemistry and mineralogy from a glacial terrain river system in southwest Iceland. Geochimica et Cosmochimica Acta, 263, 140-166. https://doi.org/10.1016/j.gca.2019.08.003.

Torres, M. A., West, A. J., Clark, K. E., Paris, G., Bouchez, J., Ponton, C., ... & Adkins, J. F. (2016). The acid and alkalinity budgets of weathering in the Andes–Amazon system: Insights into the erosional control of global biogeochemical cycles. *Earth and Planetary Science Letters*, 450, 381-391, https://doi.org/10.1016/j.epsl.2016.06.012.

Torres, M. A., Kemeny, P. C., Lamb, M. P., Cole, T. L., & Fischer, W. W. (2020). Long-Term Storage and Age-Biased Export of Fluvial Organic Carbon: Field Evidence From West Iceland. Geochemistry, Geophysics, Geosystems, 21(4), https://doi.org/10.1029/2019GC008632.

Torssander, P. (1989). Sulfur isotope ratios of Icelandic rocks. *Contributions to Mineralogy and Petrology*, *102*(1), 18-23, https://doi.org/10.1007/BF01160187.

Vigier, N., Gislason, S. R., Burton, K. W., Millot, R., & Mokadem, F. (2009). The relationship between riverine lithium isotope composition and silicate weathering rates in Iceland. *Earth and Planetary Science Letters*, 287(3-4), 434-441, https://doi.org/10.1016/j.epsl.2009.08.026.

von Strandmann, P. A. P., Burton, K. W., James, R. H., van Calsteren, P., Gíslason, S. R., & Mokadem, F. (2006). Riverine behaviour of uranium and lithium isotopes in an actively glaciated basaltic terrain. *Earth and Planetary Science Letters*, 251(1-2), 134-147, https://doi.org/10.1016/j.epsl.2006.09.001.

von Strandmann, P. A. P., Opfergelt, S., Lai, Y. J., Sigfússon, B., Gislason, S. R., & Burton, K. W. (2012). Lithium, magnesium and silicon isotope behaviour accompanying weathering in a basaltic soil and pore water profile in Iceland. *Earth and Planetary Science Letters*, 339, 11-23, https://doi.org/10.1016/j.epsl.2012.05.035.